Progress In Electromagnetics Research C, Vol. 157, 129–138, 2025

PIER C

(Received 21 May 2025, Accepted 23 June 2025, Scheduled 8 July 2025)

High-Isolation Ultra-Wideband MIMO Antenna Based on Sunflower-Shaped Radiating Patch and Defected Ground Structure

Qingqing Zhou[1], Zhonggen Wang[1,*], Wenyan Nie[2], Chenlu Li[3],
Yiwei Tao[1], and Wanying Ren[1]

[1]*School of Electrical and Information Engineering, Anhui University of Science and Technology, Huainan 232001, China*
[2]*School of Mechanical and Electrical Engineering, Huainan Normal University, Huainan 232001, China*
[3]*School of Electrical and Information Engineering, Hefei Normal University, Hefei 230061, China*

ABSTRACT: This paper presents a compact four-port ultra-wideband (UWB) multiple-input multiple-output (MIMO) antenna with exceptional isolation characteristics, specifically designed for high-frequency band communications. The antenna features a sunflower-shaped radiating patch and an irregularly stepped rectangular ground structure, which are optimized to achieve broadband impedance matching and low coupling. With dimensions of $1.26\lambda_0 \times 1.26\lambda_0 \times 0.025\lambda_0$, the antenna operates across 5.4–20 GHz, covering C-band (4–8 GHz), X-band (8–12 GHz), and Ku-band (12–18 GHz), while supporting multi-band communication compatibility. Simulation and measurement results show a return loss ($|S_{11}|$) below -10 dB over the entire frequency range, with a fractional bandwidth of 109.5%. The inter-port isolation (S_{12}) exceeds -20 dB across the band and reaches -30 dB in the high-frequency range (10–20 GHz). The antenna exhibits a radiation efficiency exceeding 80%, a peak gain of 9.3 dBi, an envelope correlation coefficient (ECC) below 0.008, a total active reflection coefficient (TARC) below -30 dB, and a group delay less than 2.3 ns, thereby meeting the stringent requirements for MIMO systems. This design offers a high-performance solution for applications in 5G, satellite, and radar communications, which combines wide bandwidth, high isolation, and low coupling in a compact form factor. The 5.4–20 GHz antenna bandwidth supplements 5G/6G applications which caters to multi-scenarios of Wi-Fi and satellite communications and facilitates signal reception and preprocessing in LEO satellite systems.

1. INTRODUCTION

With the rise of emerging fields such as the Internet of Things (IoT) and smart cities, the demand for wireless communication systems is increasing rapidly. As one of the most important components of the communication system, MIMO antenna technology has undergone continuous innovation, such as massive MIMO, software-defined MIMO, and other new technologies which have gradually become research hotspots [1]. With the advancement of semiconductor processes, the integration level of MIMO antenna systems is constantly improving. Multiple antenna units can be integrated on a single chip, thereby reducing the cost and volume while improving the reliability of the system. With the advancement of 5G and 6G communication technologies, MIMO antennas are expanding to higher frequency bands to meet the requirements of beamwidth, gain, and noise figure in higher frequency band communications. UWB antennas are rapidly developing as a promising technology operating over an extremely wide bandwidth, and UWB technology supports a variety of wireless personal area network (WPAN) applications.

Compared with traditional narrowband antennas, UWB antennas can support extremely wide frequency bands, thus achieving high data transmission rates [2, 3]. UWB technology exhibits three distinctive advantages: exceptionally low power spectral density, remarkable interference immunity, and superior low-probability-of-intercept characteristics. These inherent features, combined with the UWB antenna's compact design that enables seamless integration into miniaturized devices, have positioned UWB as a pivotal technology for modern wireless communication and precision positioning systems. With its unique combination of technical merits, UWB is set to play an increasingly vital role across diverse applications such as smart home systems, industrial IoT, and connected vehicle ecosystems. The combination of UWB and MIMO technologies offers significant advantages: increasing data transmission rate, enhancing multipath interference resistance, improving system reliability and security, boosting positioning accuracy, and optimizing spectrum utilization efficiency. These advantages collectively enhance the performance of wireless communication systems, where all antennas satisfy a fractional bandwidth requirement higher than 20%. Antennas with such characteristics include single-port subunits [11, 12], dual-port subunits [13–16], and multi-port subunits [4–10], all of which exhibit a fractional bandwidth exceeding 20% [4–16]. Antenna systems enhance wireless signal reliability and quality through spatial multiplexing and diversity. Four-port antennas leverage spatial differences among multiple antennas

---

* Corresponding author: Zhonggen Wang (zgwang@ahu.edu.cn).

doi:10.2528/PIERC25052103

Published by THE ELECTROMAGNETIC ACADEMY

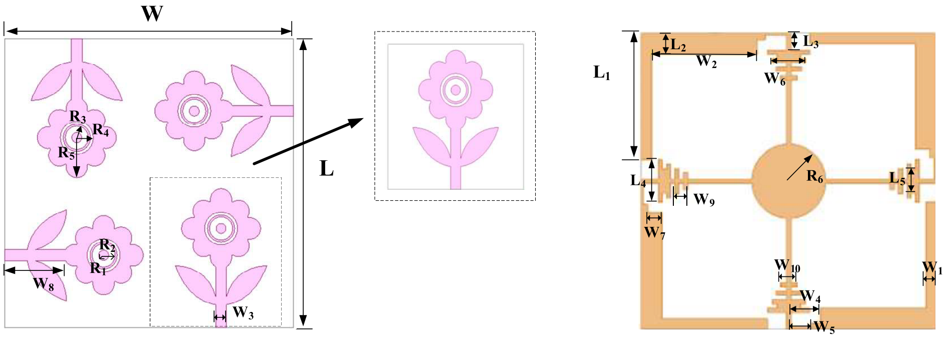

FIGURE 1. Geometry of the four-port MIMO antenna.

for diversity transmission/reception, reducing signal fading, improving stability and anti-interference capability, while minimizing coverage blind spots for uniform signal distribution. Additionally, optimized antenna layout and beamforming direct signals precisely to user areas, boosting signal strength and communication quality for edge users.

However, due to electromagnetic field interactions, when two or more antenna pole subunits are in close proximity, their fields interfere, leading to energy transfer between antennas and causing coupling [17]. This coupling stems from multiple factors: near-field coupling, surface wave coupling, mutual impedance coupling, radiated field coupling, feed network coupling, ground plane coupling, frequency coupling, and directional pattern coupling. Antenna coupling severely impacts system performance, resulting in gain degradation, directional pattern distortion, channel capacity reduction, and other issues. Thus, mitigating coupling between antenna elements is critical. To address this challenge, decoupling techniques are employed. These techniques serve as a critical approach to mitigate mutual interference (coupling) in multi-antenna systems and enhance isolation, including measures like increasing inter-antenna spacing, implementing polarization diversity [18], designing decoupling networks [19], introducing defected ground structures (DGS) [20, 21], electromagnetic bandgap (EBG) structures [22], etc. In [23], a broadband circularly polarized four-element MIMO antenna etched on a metal ground plane is proposed, which mitigates inter-element coupling via a positive-shaped decoupling structure (PSDS). However, the four-port MIMO antenna developed in [23] exhibits a relatively narrow bandwidth (3.4–8.25 GHz) due to its simplistic structural design. Ref. [24] presents an ultra-wideband (UWB) MIMO antenna based on dual-mode transmission line feeding for wireless communications. The four-port MIMO antenna covers 2.40–25 GHz, but its relatively large size restricts application scenarios.

With the growing demand for high-frequency communications (e.g., satellite, 5G, radar) and the signal crosstalk issue arising from insufficient isolation in multi-antenna systems, the research on wideband antennas has become increasingly urgent. Thus, this paper focuses on designing a compact four-port UWB MIMO antenna with high isolation characteristics in the 5.4–20 GHz band. The investigated frequency band spans the upper C-band, X-band, and Ku-band, and is extended to 20 GHz at high frequencies to enable multi-band compatibility. Additionally, it exhibits excellent radiation characteristics and diversity performance.

2. ANTENNA DESIGN

2.1. Antenna Model

The geometry of the antenna is depicted in Figure 1. The antenna is fabricated on an FR4 dielectric substrate with dimensions of $70\,\text{mm} \times 70\,\text{mm} \times 1.4\,\text{mm}$, where the relative permittivity (ε_r) is 4.4, and the loss tangent $(\tan\delta)$ is 0.02. Each antenna unit consists of a sunflower-shaped radiating patch on the top layer and an L-shaped metal ground plane on the bottom layer. The sunflower-shaped radiating patch is printed on the substrate's top surface, while the bottom L-shaped ground plane is uniformly designed to ensure that all antenna units share identical geometric shapes and orthogonal arrangements, thereby enhancing inter-unit isolation and structural compactness. Additionally, a cross-knot structure is integrated at the center of the substrate's bottom layer, which features a trapezoidal patch with a gradually tapered width at its end. The base of this trapezoidal patch is connected to an irregular stepped rectangle, which effectively improves the isolation between antenna units. Table 1 shows the dimensions of the proposed antennas.

TABLE 1. Optimized parametric dimensions of proposed MIMO antenna.

Parameters	L	L_1	L_2	L_3	L_4	L_5	W	W_1
Value (mm)	70	30	5	4	10	5.6	70	2.5
Parameters	W_2	W_3	W_4	W_5	W_6	W_7	W_8	W_9
Value (mm)	25	2.6	7	3	8	2.5	15	3
Parameters	W_{10}	R_1	R_2	R_3	R_4	R_5	R_6	
Value (mm)	4	1.2	2.8	3.3	4	2.6	8.8	

2.2. Analysis of Antenna Structure Design

2.2.1. Evolution Process of Antenna Design

Figure 2 shows the monopole structure of the proposed antenna model, and Figure 3 displays the simulation results and

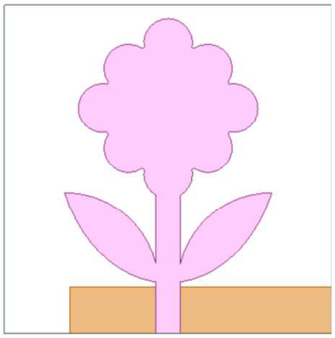

FIGURE 2. The monopole model of the proposed antenna.

radiation characteristics of the monopole model. The proposed MIMO antenna is formed by rotating the monopole antenna and evolved from it through rotational symmetry. The evolutionary process of the antenna structure is illustrated in Figure 4. As depicted in Figure 4(a), four identical flower-shaped antenna units are printed on the substrate's top layer and arranged orthogonally. An L-shaped ground plane corresponding to each radiating patch is positioned at the substrate's bottom, forming the antenna's basic structure. The resonant frequency of the patch can be calculated using the following formula:

$$f = \frac{c}{4L\sqrt{\varepsilon_r}} \tag{1}$$

where ε_r is the dielectric constant of FR4, f the center frequency, L the effective length of the rectangular patch, and c the electromagnetic wave propagation speed.

As shown in Figure 4(b), the bandwidth enhancement of the radiating patch unit is insignificant, so the antenna patch structure is modified to improve its bandwidth performance. Elliptical notches and two circular-cut irregular branch-leaf patches are introduced to the radiating patch. Additionally, a cross structure is embedded at the substrate's bottom center to enhance inter-antenna isolation. The radius (R) of the circular patches can be calculated using the following equation [22]:

$$F = \frac{8.791 \times 10^9}{f_s\sqrt{\varepsilon_r}} \tag{2}$$

$$R = \frac{F}{\left\{1 + \frac{2h}{\pi F \varepsilon_r}\left[\ln\left(\frac{\pi F}{2\pi}\right) + 1.7726\right]\right\}^{\frac{1}{2}}} \tag{3}$$

where h is the thickness of the dielectric substrate, ε_r the relative permittivity, and f_s the intended resonant frequency of the center frequency.

As shown in Figure 4(c), to extend the high-frequency bandwidth and further improve low-frequency isolation, the patch structure at the substrate's bottom is modified by incorporating irregular rectangular patches and connecting them to the cross-tail in a ladder-like configuration. The additional radiating patch alters the antenna's current distribution to achieve superior impedance matching. The patch length can be calculated using the following formula, where L_s denotes the length of the additional rectangular patch.

$$W_S = W_4 - W_5 \tag{4}$$

The S-parameters of the evolutionary antenna structures are depicted in Figure 5. Figure 5(a) shows that with the continuous evolution of the antenna structure, the antenna's effective bandwidth is broadened, ultimately expanding to 5.4–20 GHz, with the return loss significantly improved. Figure 5(b) illustrates that with the continuous evolution of the patch structure on the substrate's bottom, the low-frequency isolation performance is enhanced, with the inter-port isolation of each antenna unit ultimately reduced to below -20 dB across the operating band and below -30 dB in the 10–20 GHz range, enabling high isolation performance.

2.2.2. Antenna Parameters Analysis

To optimize the performance of the designed UWB MIMO antenna, High Frequency Structure Simulator (HFSS) simulations for parameter optimization were conducted during the design phase. The optimization strategy involves tuning one parameter while maintaining others constant. Figure 6 illustrates the optimization results. Figures 6(a)–(c) reveal that parameters R_6, W_3, and W_s primarily influence the antenna's mid-band reflection coefficients and high-band resonant frequencies. As R_6 increases, the mid-band return loss first increases then decreases, with the optimal performance attained at $R_6 = 8.6$ mm. With the gradual increase of W_3, the low/mid-band return loss significantly increases, and the low-frequency resonant frequency shifts upward, achieving the best result at $W_3 = 2.6$ mm. As W_s increases, the high-frequency resonant frequency first shifts downward then upward, while the high-band return loss exhibits a decreasing-then-increasing trend. For the low-frequency band, the return loss ($|S_{11}|$) first decreases then increases with R_6, W_3, and W_s, indicating that optimal parameter values can improve low-band impedance matching. Thus, the optimized parameters are finalized as: $R_6 = 8.6$ mm, $W_3 = 2.6$ mm, $W_s = 4$ mm.

2.2.3. Antenna Surface Current Analysis

To visualize the isolation performance of the bottom substrate structure, we analyze the current distribution at three resonant points (5.7 GHz, 8.4 GHz, 16.5 GHz, corresponding to Figures 7(a)–(c)) and its impact on inter-antenna isolation.

At 5.7 GHz (low-frequency, Figure 7(b)), exciting port 1 causes significant current coupling to port 2, evidenced by strong current paths between them. Dark regions (high current density) concentrate between these ports, while ports 3–4 show negligible current flow, indicating the structure blocks non-adjacent port coupling effectively. At 8.4 GHz (mid-frequency, Figure 7(a)), trace current coupling appears in ports 2–4. Current distribution is more dispersed with weaker intensity and fragmented paths, showing that the isolation structure mitigates coupling across multiple ports, enhancing mid-frequency signal integrity. At 16.5 GHz (high-frequency, Figure 7(c)), isolation is optimal: current localizes near port 1 with minimal coupling to other ports. High-current regions cluster tightly around the excited port, demonstrating that the structure confines current effectively, critical for MIMO performance in high-frequency applications.

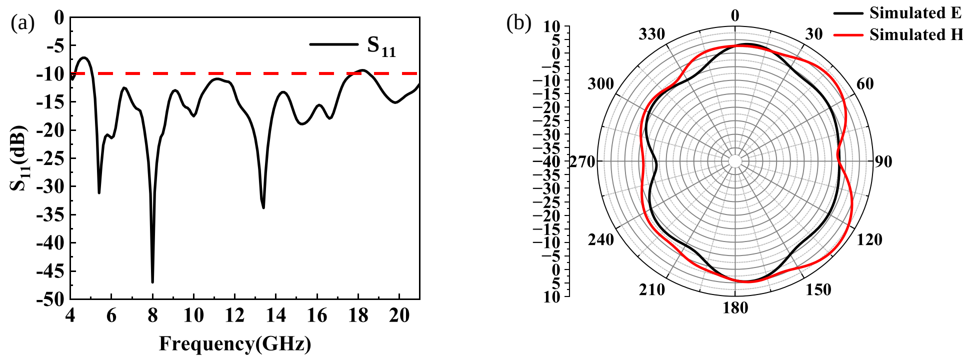

FIGURE 3. Simulation results of the monopole antenna model (a) $|S_{11}|$ and (b) radiation characteristics.

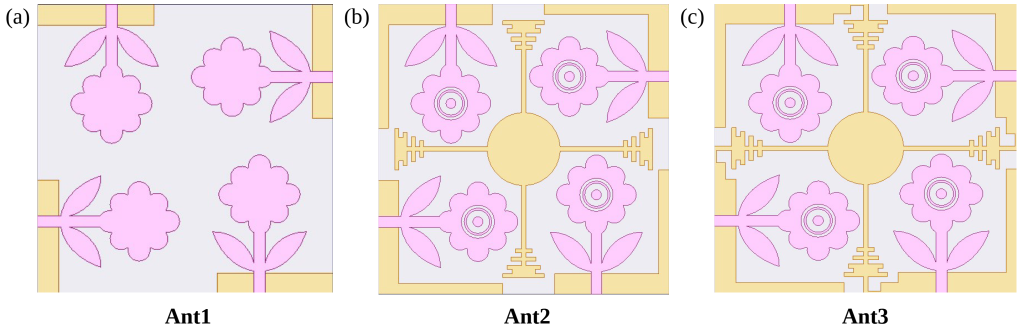

FIGURE 4. Evolutionary process of antenna structure: (a) Ant 1, (b) Ant 2, and (c) Ant 3.

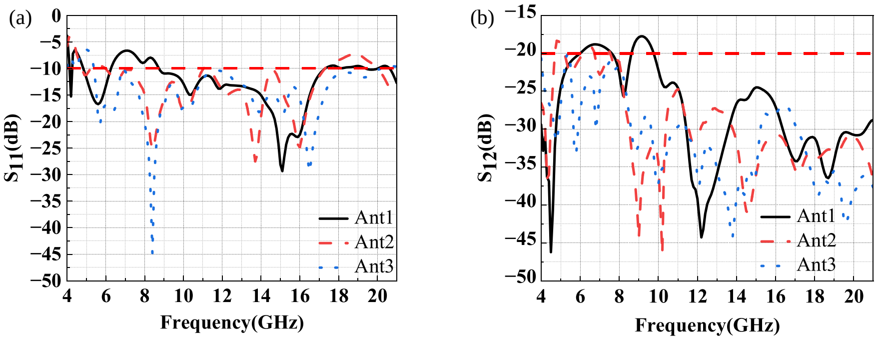

FIGURE 5. Simulation of S parameters of 3 antenna structures (a) $|S_{11}|$ and (b) S_{12}.

In summary, the bottom substrate isolation structure exhibits frequency-dependent performance, improving isolation from low to high frequencies. This behavior optimizes MIMO system performance across the entire operating band for diverse communication requirements.

3. PARAMETER SIMULATION AND MEASUREMENT

3.1. S-Parameters

The S-parameters of the antenna were measured using an Agilent N5235A vector network analyzer, and the measurement setup and physical prototype are depicted in Figure 8. Figure 9(a) shows that the $|S_{11}|$ measurements of the antenna are in good agreement with simulations, covering the required 5.4–20 GHz bandwidth. The discrepancies between measurements and simulations can be attributed to SMA connector losses, transmission line losses, or test environment errors, which result in slight frequency shifts in the measured data. Further analyzing the antenna isolation, as shown in the S_{12} parameter curve in Figure 9(b), the antenna exhibits isolation below -20 dB across the required bandwidth, confirming the high port isolation of this MIMO antenna.

3.2. Radiation Properties

The two-dimensional radiation patterns of the MIMO antenna's port 1 E-plane and H-plane at 5.7 GHz, 8.4 GHz, and 16.5 GHz are measured and depicted in Figure 10. As shown in Figure 10, at the 5.7 GHz resonant frequency, the antenna's E-plane radiation pattern is doughnut-shaped, whereas the H-plane pattern is heart-shaped. In the H-plane, the maximum radiation directions are distributed across 0–60°, 135–225°, and 300–360°, while the E-plane exhibits nearly omnidirectional radiation, in-

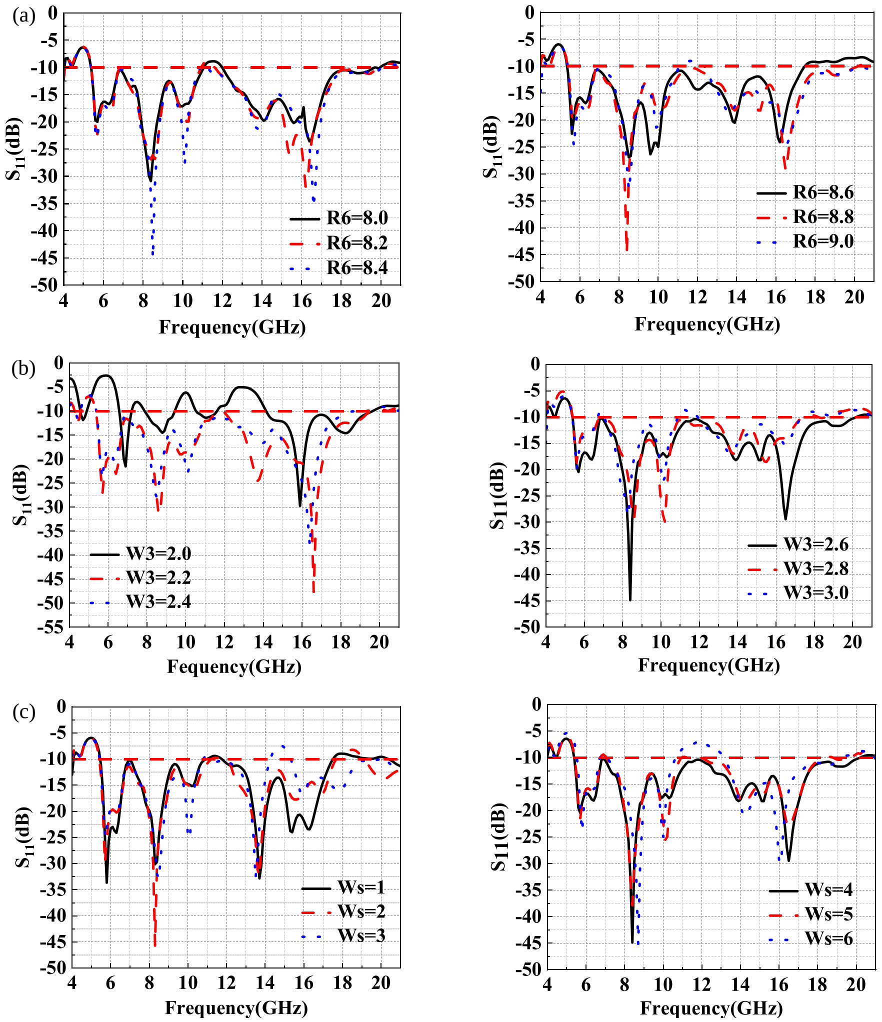

FIGURE 6. The effect of adjusted parameters on $|S_{11}|$ parameters (a) R_6, (b) W_3, and (c) W_s.

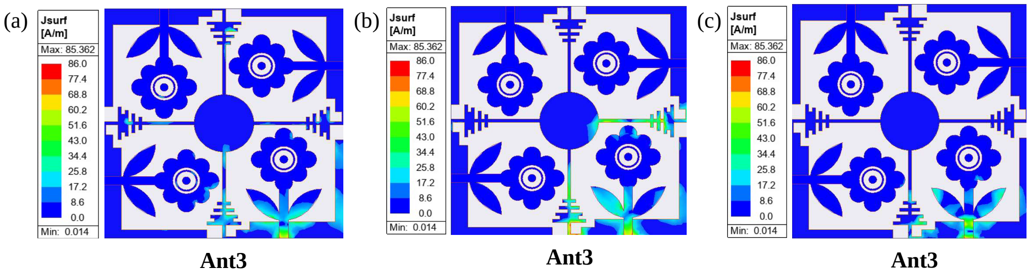

FIGURE 7. Current distribution of the third antenna at different resonant frequencies (a) 5.7 GHz, (b) 8.4 GHz, and (c) 16.5 GHz.

dicating excellent radiation directivity. At 8.4 GHz, both E-plane and H-plane exhibit figure-of-eight radiation patterns, with the H-plane's maximum radiation distributed across 0–60° and 105–180° and the E-plane showing nearly omnidirectional radiation. At 16.5 GHz, the E-plane features a butterfly-wing pattern with maximum radiation at 150–240° and 300–360°. The H-plane, conversely, exhibits a flower-like twisted pattern, with more prominent radiation gain across 165–210°, 255–285°, and 330–360°, demonstrating strong directional radiation. Overall, the antenna demonstrates robust radiation performance and high gain at all resonant frequencies, confirming its superior radiation characteristics. Figure 11 illustrates the antenna's 3D radiation patterns at various resonant frequencies, while Figure 12 depicts the 3D radiation characteristics under four-port common feeding at different frequencies.

Figure 13 illustrates the antenna's radiation efficiency and peak gain across the operating band. The antenna's peak gain ranges from 0 to 9.3 dBi. Furthermore, the antenna's radiation efficiency exceeds 80% across almost all bands and reaches over 90% in the 5.8–6.5 GHz, 7.1–10.2 GHz, and 14.1–14.6 GHz bands.

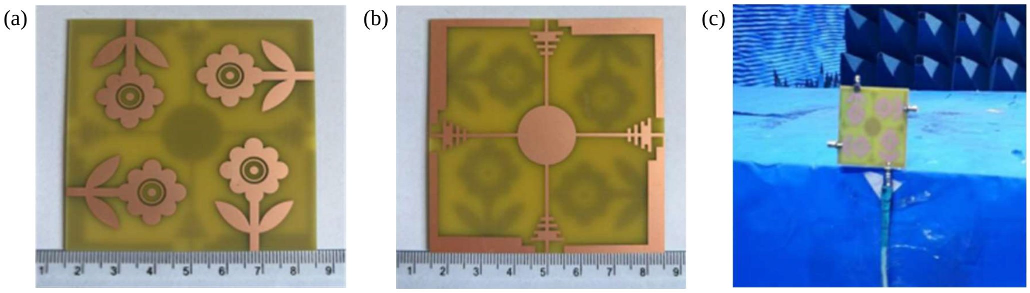

FIGURE 8. The proposed antenna fabricated prototype (a) front view, (b) back view, and (c) measurement environment.

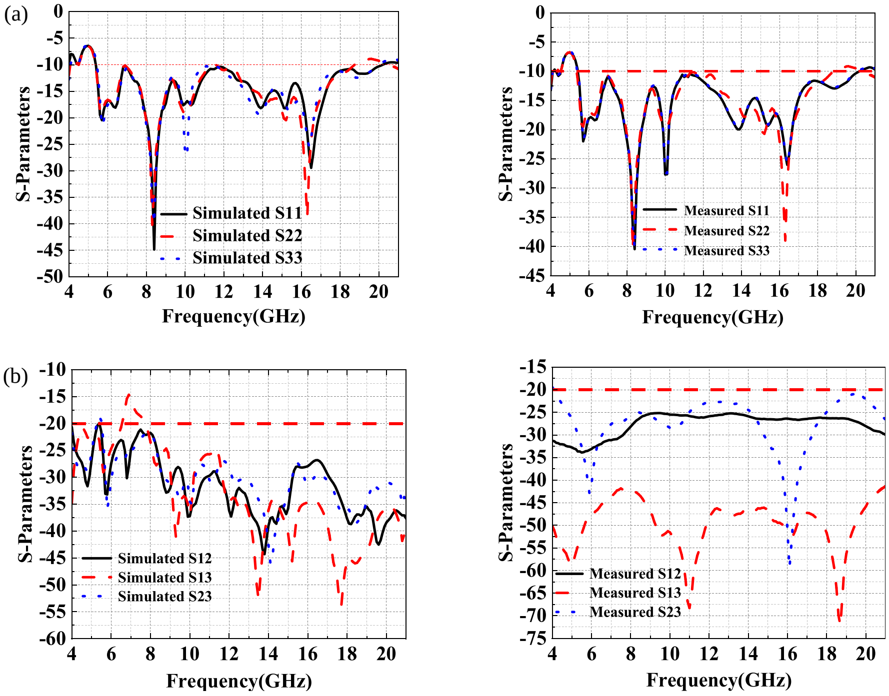

FIGURE 9. Simulated and measured S-parameters of the MIMO antenna: (a) $|S_{11}|$, (b) S_{12}.

3.3. MIMO Diversity Performance

3.3.1. ECC

The effectiveness of antenna diversity is evaluated using Envelope Correlation Coefficient (ECC), which quantifies channel isolation in wireless communication links. As per industry standards, MIMO antenna elements must meet the ECC < 0.5 criterion. The ECC can be calculated from the S-parameters using the following equation [17]:

$$\mathrm{ECC}_{ij} = \frac{\left|S_{ii}^{*}S_{ij} + S_{ji}^{*}S_{jj}\right|^2}{\left(1 - |S_{ii}|^2 - |S_{ji}|^2\right)\left(1 - |S_{jj}|^2 - |S_{ij}|^2\right)} \tag{5}$$

where ECC_{ij} is the ECC between the ith and jth antenna elements. The ECC values of the proposed UWB MIMO antenna are shown in Figure 14. In this band, the ECC between two neighboring antenna elements is less than 0.007, and the ECC between two diagonally placed antenna elements is less than 0.008, which satisfies the communication requirement of the envelope coefficient between antenna elements of less than 0.05.

3.3.2. TARC

Total active reflection coefficient (TARC) is a metric employed to assess the overall reflection performance of MIMO antennas. It comprehensively takes into consideration the reflected signals at all ports and the mutual coupling between antenna elements. The core concept involves calculating, under all-port excitation, the ratio of total reflected power to total incident power in the system, thereby reflecting the antenna's overall impedance matching efficiency. Ideally, TARC should approach zero, signifying that the antenna absorbs all incident power. The TARC of this MIMO system can be calculated via the following formula:

$$\mathrm{TARC}_{ij} = \sqrt{\frac{\left(S_{ii} + S_{ij}\right)^2 + \left(S_{ji} + S_{jj}\right)^2}{2}} \tag{6}$$

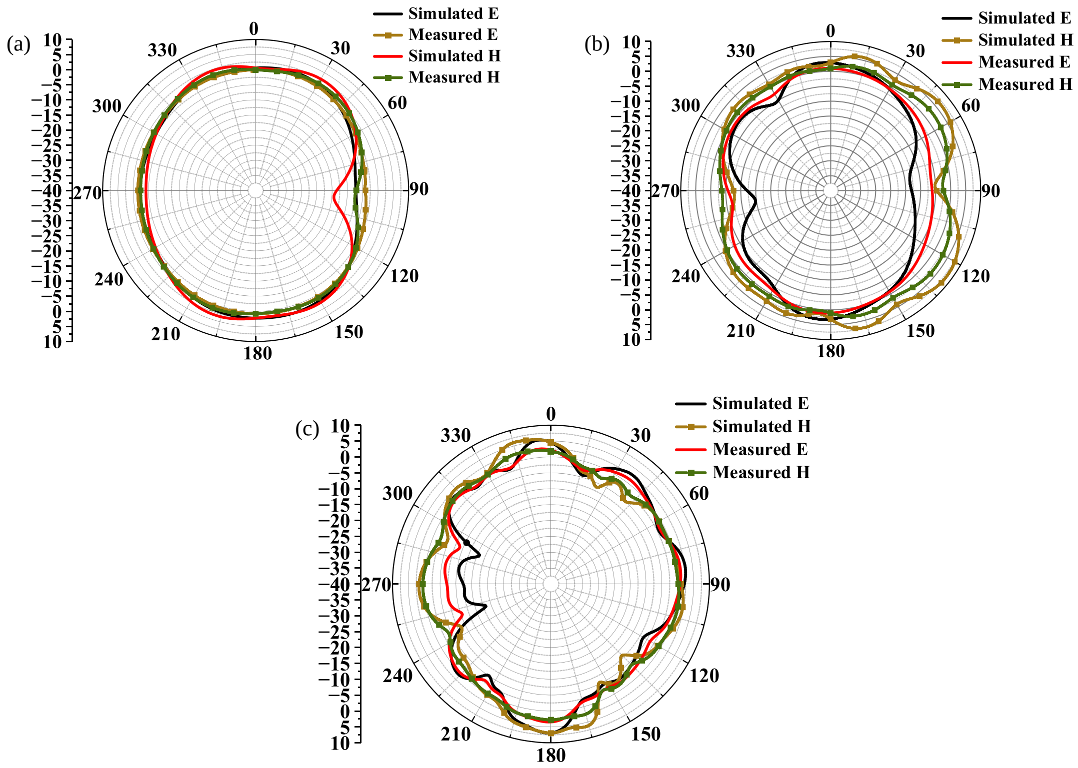

FIGURE 10. Modelled and measured radiation characteristics at (a) 5.7 GHz, (b) 8.4 GHz, and (c) 16.5 GHz.

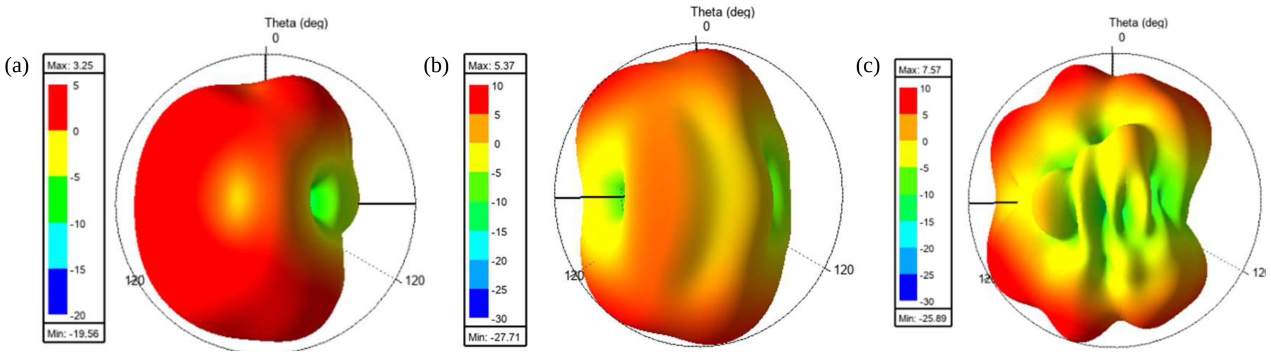

FIGURE 11. 3D radiation characteristics of the antenna at (a) 5.7 GHz, (b) 8.4 GHz, and (c) 16.5 GHz.

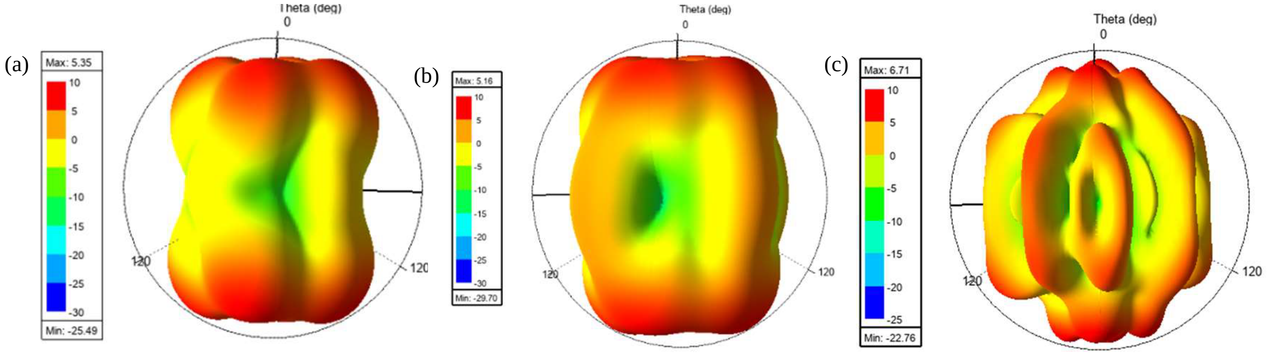

FIGURE 12. 3D radiation characteristics of the four-port co-fed antenna at (a) 5.7 GHz, (b) 8.4 GHz, and (c) 16.5 GHz.

where TARC_{ij} is the TARC between the ith and jth antenna elements. When considering the mutual coupling effect between antenna units, it is necessary to achieve the index requirement of TARC below -10 dB in the operating frequency band. As shown in Figure 15, the TARC is lower than -30 dB in the operating frequency band 5.4–20 GHz and reaches below -40 dB in 8–20 GHz.

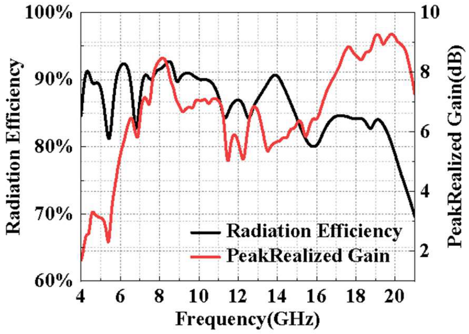

FIGURE 13. Simulation results of the radiation efficiency and peak realized gain of the proposed antenna.

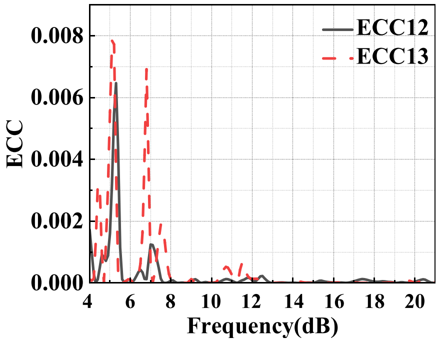

FIGURE 14. Simulation results of ECC of the proposed antenna.

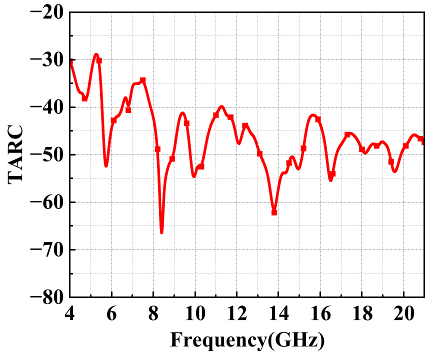

FIGURE 15. Simulation results of the TARC of the proposed antenna.

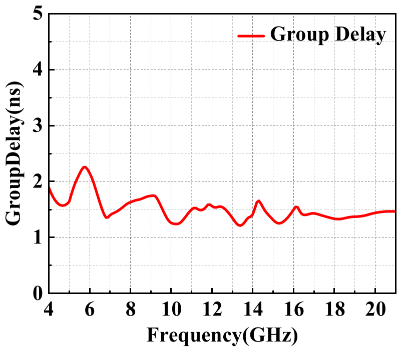

FIGURE 16. Simulation results of the group delay of the proposed antenna.

TABLE 2. Performance comparison of the proposed MIMO antenna with other works.

Ref.	Size (mm^2)	Bandwidth (GHz)	Isolation (dB)	Port	ECC
[14]	25 × 40	3.39–9.1	> 15	2	< 0.003
[15]	66 × 36	2.7–12	> 25	2	< 0.001
[17]	36 × 36	2–11.08	> 15	4	< 0.13
[23]	80 × 80	3.4–8.25	> 25	4	< 0.01
[24]	80 × 80	2.4–25	> 20	4	< 0.002
[25]	56 × 41	3.4–11.8	> 20	4	< 0.002
[26]	76 × 76	1–20	> 50	4	< 0.004
[27]	70 × 70	3.2–11.2	> 20	4	< 0.04
[27]	67 × 81	3.89–17.09	> 15	2	< 0.02
This work	70 × 70	5.4–20	> 20	4	< 0.008

3.3.3. Group Delay

Figure 16 shows the group delay characteristics of the proposed antenna. The group delay ranges from 1 to 2.5 ns with no pronounced abrupt changes (e.g., severe oscillations or sudden transitions). This demonstrates that the system effectively mitigates frequency dispersion in UWB signals (where excessive delay differences among frequency components cause pulse broadening and distortion), satisfying the demands of high-precision communication/positioning applications (e.g., UWB indoor positioning and high-speed short-range communication).

3.4. Comparative Study

Table 2 shows the detailed comparison of the size, operating frequency, isolation, number of ports, and ECC of the proposed UWB MIMO antenna with several previously published antennas. The proposed antenna provides a wider operating frequency than the previous studies available in [14–17, 23, 25, 27]. Moreover, the dimensions of the present work are also smaller than [23, 24, 26], and the isolation is better than [14, 17, 27]. Moreover, the ECC of the proposed antenna is superior compared to [17, 23, 27]. In conclusion, among the comparable performance metrics relative to other antennas, this proposed antenna demonstrates superior performance in certain aspects when being benchmarked against the reference antennas and is well suited for contemporary communication systems.

4. CONCLUSION

A compact 70 mm × 70 mm four-port UWB MIMO antenna operating at 5.4–20 GHz is presented. Isolation performance is enhanced via a flower-shaped radiating patch, defected ground structure (DGS), and orthogonal layout. The bandwidth is extended to 5.4–20 GHz using elliptical notching and a stepped ground, covering C- and Ku-bands for future high-frequency (HF) communication. The cross-knot structure and trapezoidal patch suppress surface waves, achieving < -20 dB isolation across all bands. Key metrics include ECC < 0.008, TARC < -30 dB, radiation efficiency $> 80\%$, and group delay < 2.3 ns, validating reliability in multipath scenarios. Measured results agree well with simulations. The 5.4–20 GHz antenna bandwidth supplements 5G/6G applications, caters to multi-scenarios of Wi-Fi and satellite communications and facilitates signal reception and preprocessing in LEO satellite systems.

REFERENCES

[1] Yuan, X.-T., Z. Chen, T. Gu, and T. Yuan, "A wideband PIFA-pair-based MIMO antenna for 5G smartphones," *IEEE Antennas and Wireless Propagation Letters*, Vol. 20, No. 3, 371–375, 2021.

[2] Wu, B., X.-Y. Sun, H.-R. Zu, H.-H. Zhang, and T. Su, "Transparent ultrawideband halved coplanar Vivaldi antenna with metal mesh film," *IEEE Antennas and Wireless Propagation Letters*, Vol. 21, No. 12, 2532–2536, Dec. 2022.

[3] Li, J.-F., Q.-X. Chu, Z.-H. Li, and X.-X. Xia, "Compact dual band-notched UWB MIMO antenna with high isolation," *IEEE Transactions on Antennas and Propagation*, Vol. 61, No. 9, 4759–4766, 2013.

[4] Ren, J., W. Hu, Y. Yin, and R. Fan, "Compact printed MIMO antenna for UWB applications," *IEEE Antennas and Wireless Propagation Letters*, Vol. 13, 1517–1520, 2014.

[5] Gautam, P. K. and D. K. Jhariya, "Design of a 4-element UWB-MIMO antenna for X, Ku, and, K band applications," in *2024 IEEE Wireless Antenna and Microwave Symposium (WAMS)*, 1–5, Visakhapatnam, India, 2024.

[6] Wong, K.-L., Y.-H. Hsu, C.-Y. Lee, and W.-Y. Li, "Wideband 4-port patch antenna module based compact 8-port two-module antenna for 6G upper mid-band 8 × 4 device MIMO with enhanced spectral efficiency," *IEEE Access*, Vol. 12, 88 976–88 991, 2024.

[7] Shabbir, T., R. Saleem, S. S. Al-Bawri, M. F. Shafique, and M. T. Islam, "Eight-port metamaterial loaded UWB-MIMO antenna system for 3D system-in-package applications," *IEEE Access*, Vol. 8, 106 982–106 992, 2020.

[8] Nie, L. Y., X. Q. Lin, S. Xiang, B. Wang, L. Xiao, and J. Y. Ye, "High-isolation two-port UWB antenna based on shared structure," *IEEE Transactions on Antennas and Propagation*, Vol. 68, No. 12, 8186–8191, 2020.

[9] Jayant, S. and G. Srivastava, "Close-packed quad-element triple-band-notched UWB MIMO antenna with upgrading capability," *IEEE Transactions on Antennas and Propagation*, Vol. 71, No. 1, 353–360, 2023.

[10] Chen, J., M. Wen, X. He, J. Xue, and X. Chen, "Compact, UWB, dual-polarized antenna based on tightly coupling effect," *IEEE Antennas and Wireless Propagation Letters*, Vol. 23, No. 10, 3292–3296, 2024.

[11] Pathak, P. A., S. L. Nalbalwar, A. E. Wagh, and J. L. Rajput, "A fractal approach to investigate SAR of HMSA UWB antenna for medical applications," *Progress In Electromagnetics Research C*, Vol. 154, 67–75, 2025.

[12] Hasan, Y. M., "A compact monopole slotted patch-antenna for UWB applications," *Progress In Electromagnetics Research C*, Vol. 151, 65–71, 2024.

[13] Khedr, A. A., B. E. Elnaghi, and A. M. Mohamed, "Design of a compact dual port 2 × 1 ultra-wideband MIMO antenna for radio frequency energy harvesting based on four "a" shaped slots," *Progress In Electromagnetics Research M*, Vol. 128, 41–49, 2024.

[14] Haripriya, D., S. Venkatakiran, and A. Gokulachandar, "UWB-MIMO antenna of high isolation two elements with WLAN single band-notched behavior using roger material," *Materials Today: Proceedings*, Vol. 62, 1717–1721, 2022.

[15] Wang, Z., G. Song, W. Nie, M. Yang, C. Li, and M. Wang, "A racket-like UWB MIMO antenna with high isolation," *Progress In Electromagnetics Research C*, Vol. 144, 159–168, 2024.

[16] Ren, W., Z. Wang, M. Yang, J. Zhou, and W. Nie, "Design of a simple four-port UWB-MIMO antenna based on a fan-shaped isolator," *Progress In Electromagnetics Research M*, Vol. 126, 117–126, 2024.

[17] Wu, B. and K.-M. Luk, "A UWB unidirectional antenna with dual-polarization," *IEEE Transactions on Antennas and Propagation*, Vol. 59, No. 11, 4033–4040, 2011.

[18] Yang, M., C. Liu, and X. Liu, "Design of π-shaped decoupling network for dual-polarized Y-probe antenna arrays," *IEEE Antennas and Wireless Propagation Letters*, Vol. 21, No. 6, 1129–1133, 2022.

[19] Wang, F.-W., Y. Liu, S.-X. Gong, and R.-X. Liang, "Employing DGS structures in dual-band antennas for MIMO applications with high port isolation," in *IET International Radar Conference 2013*, E0230, Xi'an, China, Apr. 2013.

[20] Kumar, P., S. Pathan, S. Vincent, O. P. Kumar, P. Kumar, *et al.*, "A compact quad-port UWB MIMO antenna with improved isolation using a novel mesh-like decoupling structure and unique DGS," *IEEE Transactions on Circuits and Systems II: Express Briefs*, Vol. 70, No. 3, 949–953, 2023.

[21] Fitri, A., U. Umaisaroh, and M. Alaydrus, "A novel parasitic EBG structure to enhance mutual coupling for 2.45 GHz MIMO antenna," in *2022 International Conference on Radar, Antenna, Microwave, Electronics, and Telecommunications (ICRAMET)*, 253–257, Bandung, Indonesia, 2022.

[22] Sharma, N. and S. S. Bhatia, "Metamaterial inspired fidget spinner-shaped antenna based on parasitic split ring resonator for multi-standard wireless applications," *Journal of Electromagnetic Waves and Applications*, Vol. 34, No. 10, 1471–1490, 2020.

[23] Ghosh, A., A. Ghosh, and J. Kumar, "Circularly polarized wideband quad-element MIMO antenna with improved axial ratio bandwidth and mutual coupling," *IEEE Antennas and Wireless Propagation Letters*, Vol. 23, No. 12, 4718–4722, 2024.

[24] Lin, X., G. Huang, and Y. Zhang, "An ultra-wideband MIMO antenna based on dual-mode transmission line feeding for wireless communication," *Progress In Electromagnetics Research M*, Vol. 122, 73–83, 2023.

[25] Jhunjhunwala, V. K., P. Kumar, A. P. Parameswaran, P. R. Mane, O. P. Kumar, T. Ali, S. Pathan, S. Vincent, and P. Kumar, "A four port flexible UWB MIMO antenna with enhanced isolation for wearable applications," *Results in Engineering*, Vol. 24, 103147, 2024.

[26] Yao, Y., Y. Shao, J. Zhang, and J. Zhang, “A transparent antenna using metal mesh for UWB MIMO applications,” *IEEE Transactions on Antennas and Propagation*, Vol. 71, No. 5, 3836–3844, 2023.

[27] Desai, A., J. Kulkarni, M. M. Kamruzzaman, □. Hubálovský, H.-T. Hsu, and A. A. Ibrahim, “Interconnected CPW fed flexible 4-port MIMO antenna for UWB, X, and Ku band applications,” *IEEE Access*, Vol. 10, 57 641–57 654, 2022.